Check for updates

Multifunctional property exploration: $Bi_4O_5I_2$ with high visible light photocatalytic performance and a large nonlinear optical effect†

Ruonan Yin, Yang Li, Kangdi Zhong, Hang Yao, Yamin Zhang and Kangrong Lai [ID] *

Exploration of the versatility of materials is very important for increasing the utilization of materials. Herein, we successfully prepared $Bi_4O_5I_2$ powders *via* a facile solvothermal method. The $Bi_4O_5I_2$ photocatalyst exhibited significantly higher photocatalytic activity as compared to the common BiOI photocatalyst in the degradation of methyl orange, methylene blue and rhodamine B under visible light irradiation. Especially, for the degradation of methyl orange, the photocatalytic activity of $Bi_4O_5I_2$ is about 10 times that of BiOI. Moreover, $Bi_4O_5I_2$ exhibits an extremely high second harmonic generation response of about $20 \times$ KDP (the benchmark) estimated by the unbiased *ab initio* calculations. The coexisting multifunction of $Bi_4O_5I_2$ is mainly because of the increased dipole moment due to the stereochemical activity of lone pairs that promotes separation and transfer of photogenerated carriers, then enhances the photocatalytic activity and results in a high second harmonic generation response. This indicates that $Bi_4O_5I_2$ may have good potential applications in photocatalytic and nonlinear optical fields.

1. Introduction

Green, efficient, harmonious and civilized society is the development trend of future life. Ever since Fujishima and Honda have reported the photocatalytic water splitting on the TiO_2 surface,[1] TiO_2 has been extensively studied for the degradation of pollutants or splitting of water.[2] However, the wide bandgap (3.0–3.2 eV) of TiO_2 limits its application range. Therefore, it is essential to find visible light-driven photocatalysts. Methylene blue (MB), methyl orange (MO) and rhodamine B (RhB) are the main components in common water pollutants. Scientists have invented many methods for the degradation of organic pollutants.[3–8] Bismuth-containing materials are attracting significant attention of researchers due to their unique electronic, magnetic, optical, and catalytic properties;[9–13] however, the

Department of Physics, Changji University, 77# North Beijing Road, Changji 831100, China. E-mail: laikr0212@163.com; Tel: +86-889-9049560; +86-994-2336271

existence of high photogenerated carrier recombination rate restricts the development of Bi-based photocatalysts.

To enhance the photocatalytic activity, scientists have carried out a lot of research and exploration.[14–21] To the best of our knowledge, in 2002, $Bi_4O_5I_2$ was successfully synthesized by changing the stoichiometry of bismuth oxyhalide.[22] After this, non-stoichiometric ratio halogenated bismuth compounds, for example, $Bi_4O_5I_2$, $Bi_4O_5Br_2$, and Bi_5O_7Br, have been studied constantly.[23,24] Ye *et al.* have committed to the research and development of non-stoichiometric Bi-based photocatalysts. They made a series of innovative achievements such as photocatalytic water splitting for hydrogen (H_2) evolution,[25] selective photoreduction of CO_2 into CO,[26] molecular oxygen activation and RhB degradation.[27,28] Xiao *et al.*[29,30] have successfully synthesized $Bi_4O_5I_2$ nanoflakes, which had better photocatalytic activities in the degradation of 4-*tert*-butylphenol, and predicted that they could be applied to other fields as well.

Non-stoichiometric ratio halogenated bismuth compounds have become the most promising second-order nonlinear optical (NLO) and photovoltaic (PV) candidate materials owing to their special structural features, rich chemical compositions, and suitable optical band gaps. In fact, most of these non-centrosymmetric structures could be applied in more than one of the aforementioned fields. It is known that nonlinear optical (NLO) materials have played an important role in laser science and technology field and are rapidly developing.[31–34] The NLO crystals are laser frequency conversion materials, and their SHG coefficients are the focus of attention, which may reflect the ability of the NLO crystal to generate harmonic laser emission.[35,36] Among them, fluoroborate is responsive to ultraviolet

light and is widely used in military, medical, aviation and other fields.[37] It is known that lower SHG coefficient limits their applications. Therefore, the search for new NLO materials with SHG response larger than 10 × KDP has attracted significant attention.

In general, noncentrosymmetric crystal structure materials may possess very good NLO properties.[28] In 2014, Fan *et al.*[38–40] found a series of materials, such as $K_3B_6O_{10}Br$, $Na_3VO_2B_6O_{11}$, and $M_2B_5O_9Cl$ (M = Ca, Sr, Ba, Pb), with noncentrosymmetric structures. Due to intrinsic large polarization effects, they not only have good nonlinear optical properties, but have also been found to exhibit significantly enhanced photocatalytic activities.

To the best of our knowledge, the noncentrosymmetric polarized $Bi_4O_5I_2$ belongs to the space group $P2_1$.[22] Then, does it have the multifunctional property? To research the potential properties of $Bi_4O_5I_2$, we carried out photodegradation experiments and theoretical calculations of the optical properties. The results showed that $Bi_4O_5I_2$ had high visible light photocatalytic performance. Moreover, the theoretical calculation showed that $Bi_4O_5I_2$ exhibited large second harmonic generation (SHG) response. At present, the versatility of materials is a hot research topic that scientists have been exploring. Based on the above-mentioned findings, herein, we successfully prepared BiOI and $Bi_4O_5I_2$ materials, and some characterizations and calculations were performed to verify the versatility of these materials.

2. Experimental

2.1. Materials and methods

Ethylene glycol (EG), bismuth nitrate pentahydrate ($Bi(NO_3)_3 \cdot 5H_2O$), and potassium iodide (KI) were purchased commercially and used without further purification. Moreover, deionized water was used throughout this study.

$Bi_4O_5I_2$ powders were synthesized *via* a facile solvothermal method. A mixture of 2 mmol $Bi(NO_3)_3 \cdot 5H_2O$, 4 mmol KI and 35 mL EG was prepared and transferred to a 45 mL Teflon-lined stainless steel autoclave, and the pH of the suspension was adjusted to 10 using 2 mol L^{-1} NaOH. Subsequently, it was maintained at 150 °C for 12 h followed by naturally cooling to room temperature. The precipitate was centrifugally washed with distilled water and absolute ethanol for several times and then dried at 80 °C for 5 h under an air atmosphere. BiOI was obtained through the abovementioned procedure without the addition of NaOH.

2.2. Characterization

Phase identification was performed using the Bruker D8 ADVANCE X-ray diffractometer (XRD) equipped with a dif-fracted-beam monochromator set for Cu and Kα (λ = 0.154059 nm) as the radiation sources. The acceleration voltage and acceleration current are 40 kV and 40 mA, respectively. The results were obtained by scanning the sample through a range of 2 theta values (10–85°). UV-visible diffuse reflectance spectra (DRS) were obtained *via* the Shimadzu UV-3600 UV-vis spectrophotometer using $BaSO_4$ as a reference. The morphologies of the samples were observed *via* a scanning electron microscope

(SEM) using a Zeiss SUPRA 55VP apparatus, and energy dispersive X-ray (EDX) spectroscopic analysis was conducted using EDX-8000. The photocurrents (PC) of UV-vis light on and off studies were measured *via* the CHI660E electrochemical system (Shanghai, China) using a standard three-electrode cell containing a working electrode (1.0 cm × 1.0 cm), a platinum plate as the counter electrode, and a standard calomel electrode (SCE) as the reference electrode. Electrochemical impedance spectroscopy (EIS) measurements were carried out using an electrochemical workstation (Zahner Im6ex) with the working electrode in the frequency range from 100 kHz to 0.01 Hz at open circuit potential in a 0.1 M KCl solution.

2.3. Photocatalytic reaction

The photocatalytic activities of BiOI and $Bi_4O_5I_2$ samples were tested using a 300 W Xe lamp as the light source and by the degradation of MO, MB, RhB and norfloxacin (NOR) under the visible-light irradiation. Optical filters were used to eliminate the UV light ($\lambda \leq 420$ nm). The power density at the position of the reactor is about 7.4 mW cm^{-2}. In each of the experiment, 50 mg catalyst powder was dissolved in an aqueous solution of MO (100 mL, 10 mg L^{-1}) in a beaker. Prior to irradiation, the suspensions were magnetically stirred in the dark for 30 min to achieve an adsorption–desorption equilibrium. Reduction in the concentrations of dyes was analyzed by the Cary 500 UV-vis spectrophotometer at the wavelength of maximal absorption (464 nm, 664 nm, and 554 nm). The samples of the reaction solution were taken out and then centrifuged and filtered at regular intervals. Finally, the filtrates obtained were analyzed.

2.4. Numerical calculation details and methods

The electronic structures and NLO properties of BiOI and $Bi_4O_5I_2$ were simulated by the CASTEP package.[41] The experimental crystal data were used in density functional theory (DFT) calculation *via* a plane wave pseudo-potential method. During the calculation, geometry optimization was performed using the BFGS minimization technique. The local density approximation (LDA) with the Ceperley–Alder–Perdew–Zunger functional and the ultrasoft pseudopotentials (USPs) were chosen as the exchange correlation functional and pseudopotential, respectively.[42] In the electronic structure and optical property calculations, the ultra-fine pseudopotentials were set up for BiOI and $Bi_4O_5I_2$. Bi $5d^{10}6s^26p^3$, I $5s^25p^5$, and O $2s^22p^4$ were chosen as the valence electrons. The *k*-point separation of each material was set to 0.04 Å^{-1} in the Brillouin zone.

3. Results and discussion

3.1. XRD analysis

BiOI and $Bi_4O_5I_2$ belong to the tetragonal space group $P4/nmm$ with cell dimensions a = 3.995(2) Å, b = 3.995(2) Å, and c = 9.151(5) Å and noncentrosymmetric monoclinic space group $P2_1$ with cell dimensions a = 14.944(1) Å, b = 5.6983(3) Å, and c = 11.263(1) Å, respectively. Powder XRD was used to characterize the crystal structure of the products. Fig. 1 shows the XRD patterns of the BiOI and $Bi_4O_5I_2$ samples. As shown in Fig. 1a,
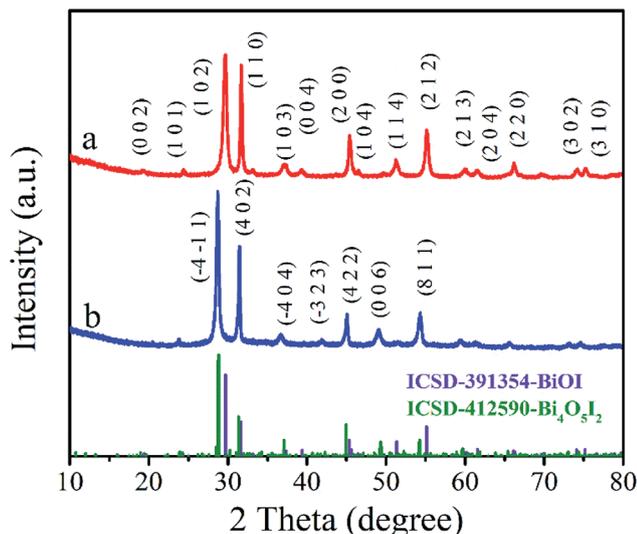
Fig. 1 XRD patterns of the BiOI (a) and $Bi_4O_5I_2$ (b) samples.

Fig. 2 SEM images of different magnifications of BiOI (a and b) and $Bi_4O_5I_2$ (c and d) samples.

Fig. 3 (a) UV-vis diffuse reflectance spectra of $Bi_4O_5I_2$ and BiOI. (b) Plots of $(\alpha h\nu)^{1/2}$ of $Bi_4O_5I_2$ and BiOI *versus* photon energy ($h\nu$).

all the observed peaks of the pattern can be indexed to the tetragonal phase of BiOI (ICSD 391354), and the observed major diffraction peaks at 29.65°, 31.66°, 45.38°, 51.35° and 55.15° belong to (102), (110), (200), (114) and (212) planes of the tetragonal phase BiOI, respectively. Fig. 1b clearly shows that the diffraction data match well with the phase of $Bi_4O_5I_2$ (ICSD 412590). Moreover, it can be clearly seen that the characteristic peaks located at 28.8, 31.5, 45.1, 49.3, and 54.4 can be indexed to (−4−11), (402), (422), (006), and (811) planes of $Bi_4O_5I_2$, respectively (Fig. 1b). These findings are consistent with the previously reported data. Therefore, it can be initially determined that BiOI and $Bi_4O_5I_2$ samples have been successfully synthesized.

3.2. SEM and EDS analyses

To identify the morphological information and atomic compositions of samples, BiOI and $Bi_4O_5I_2$ samples were investigated by SEM and EDS. The results are shown in Fig. 2. As clearly observed from Fig. 2a–d, the architecture and morphology of $Bi_4O_5I_2$ nanosheets are distinctly different from those of BiOI. The flaked structure of the $Bi_4O_5I_2$ nanosheet has been successfully prepared. The EDS results are shown in Fig. S1a and b,† and the Bi : I ratios of $Bi_4O_5I_2$ and BiOI are determined to be 2.2 : 1 and 1.08 : 1, respectively. The EDS results further demonstrate the conclusion drawn based on the XRD results.

3.3. UV-vis diffuse reflectance spectral analysis

As shown in Fig. 3a, the absorption edges of BiOI and $Bi_4O_5I_2$ samples are about 663 nm and 536 nm, respectively. The band gap energies of BiOI and $Bi_4O_5I_2$ may be determined by the following equation:[43–47]

$$\alpha h\nu = A\left(h\nu - E_g\right)^{\frac{n}{2}}$$

where α, h, $h\nu$, A, and E_g are the absorption coefficient, Planck's constant, photon energy, a constant value, and bandgap energy, respectively. In addition, n is determined by the transition type
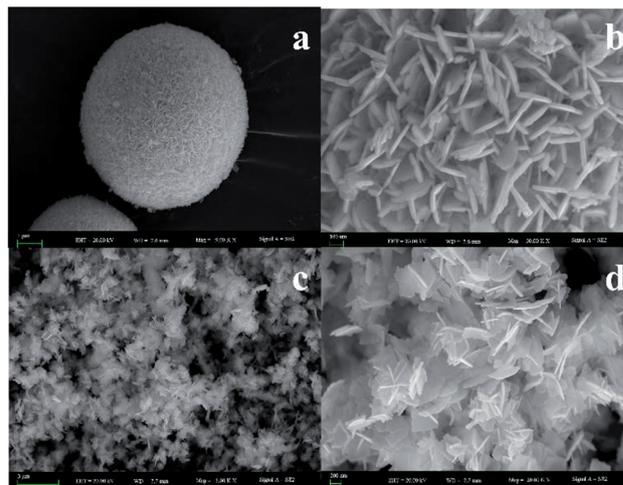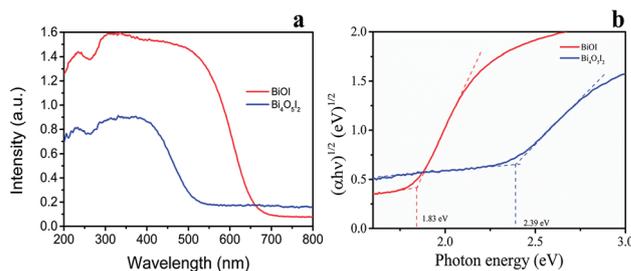
of a semiconductor ($n = 1$ for direct transition, whereas $n = 4$ for indirect transition). According to the previously reported studies,[48] the n value of BiOI and $Bi_4O_5I_2$ is 4, which is consistent with the band structure results. According to the formula, the band gap energies for BiOI and $Bi_4O_5I_2$ samples are found to be 1.83 and 2.39 eV, respectively.

3.4. Photocatalytic degradation analysis

As shown in Fig. S2a†, an adsorption–desorption equilibrium has been achieved in dark for 30 min. To better understand the photocatalytic effect of the samples, MO solutions at different initial concentrations were used for comparison. It is observed from Fig. S2b† that lower concentrations of MO degrade more efficiently. As the initial concentration of MO increases, additional organic molecules are able to adsorb onto the photocatalysts surface, thereby reducing the photogeneration of the reactive oxygen species. In addition, it can be clearly seen that $Bi_4O_5I_2$ displays relatively better degradation efficiency than TiO_2 (P25) (Fig. S2a†).

Herein, MO, RhB and MB dyes were selected as model pollutants to evaluate the photocatalytic activities of BOI and $Bi_4O_5I_2$ (Fig. S2c†). It is clearly seen that $Bi_4O_5I_2$ displays relatively better degradation efficiency than BiOI. Moreover, as can be seen, under the light irradiation for 100 min, about 29%,

50%, and 90% of RhB, MO and MB were degraded over the BOI samples, respectively. However, under the light irradiation for 60 min, 94% of MO and MB were degraded over the $Bi_4O_5I_2$ samples. Note that under the light irradiation for 40 min, 99% of RhB was degraded over the $Bi_4O_5I_2$ samples. In Table ESI-1,† the results show that the photocatalytic activity of the $Bi_4O_5I_2$ photocatalyst is about 10 times that of BiOI for the degradation of MO. In addition, to minimize the effect of dye sensitization, degradation of colorless solution has been performed (Fig. S2d†). As can be seen, under light irradiation for 100 min, about 43% of NORs were degraded over the $Bi_4O_5I_2$ samples.

3.5. Free-radical trapping experiment analysis

Trapping experiments may confirm the main active species during the photodegradation process.[4,30] Ar, IPA, and KI purging were employed to quench the active species such as $\cdot O^{2-}$, $\cdot OH$ and h^+, respectively. At first, trapping agents were dissolved in a $Bi_4O_5I_2$ solution before the reaction. The free-radical trapping experiment results are shown in Fig. S3a.† It can be seen that the photoinduced h^+ and $\cdot O^{2-}$ radicals are the primary reactive species. To evaluate the repeatability of the $Bi_4O_5I_2$ sample, recycling experiments for the photocatalytic degradation of MO over the $Bi_4O_5I_2$ sample were performed (Fig. S3b†). Note that even after 4 cycles, the photocatalytic performance of $Bi_4O_5I_2$ was retained. These results imply the high stability of the $Bi_4O_5I_2$ sample, which is significant for its practical application.

3.6. Band structure analysis

The electronic structures of BiOI and $Bi_4O_5I_2$ were calculated. As shown in Fig. 4a, the highest valence band (VB) is located between the R and Z points and the lowest conduction band (CB) is located between Γ and Z points for BiOI. As shown in Fig. 4b, the highest valence band (VB) is located between D and E points and the lowest conduction band (CB) is located at Γ point for $Bi_4O_5I_2$. Therefore, the calculated indirect band gaps of BiOI and $Bi_4O_5I_2$ are about 1.65 and 2.34 eV, which are close to the experimental values of 1.83 and 2.39 eV, respectively.

3.7. Dipole moment analysis

To identify what promotes the effective separation of photo-generated electron–hole pairs of $Bi_4O_5I_2$, the dipole moment calculation was carried out.[39] The calculations of the Bi–O and Bi–I bond valences and dipole moments of the BiO_mI_n ($m = 4, n = 4$; $m = 5, n = 3$; $m = 6, n = 1$; $m = 3, n = 4$; $m = 3, n = 5$) polyhedra in $Bi_4O_5I_2$ were performed. The details of the calculations are also

provided in ESI.† The results and details of the calculations are provided in Table ESI-2.† It proves that the direction of the dipole moment of $Bi_4O_5I_2$ powder is along [0 −1 0]. Due to the increased dipole moments, $Bi_4O_5I_2$ has better separation efficiency of electron–hole pairs. The polarization promotes the separation of photogenerated electron–hole pairs and mitigates the charge recombination, thus resulting in high photocatalytic activity. The calculated results are in accordance with those obtained *via* the photocatalytic degradation experiments.

3.8. PC and EIS analyses

The separation of photoinduced electron–hole pairs and the charge transfer processes in $Bi_4O_5I_2$ were investigated by transient photocurrent (TPC) response and electrochemical impedance spectra (EIS), respectively. Fig. 5a shows the instantaneous photocurrent response of BiOI and $Bi_4O_5I_2$ catalysts. As can be seen from Fig. 5a, due to the action of dipole moments, the photocurrent of $Bi_4O_5I_2$ is significantly higher than that of BiOI, which promotes the effective separation of photogenerated carriers, thereby resulting in an increase in photocurrent. To better understand the PC measurement results, the EIS spectrum in the form of a Nyquist plot are shown in Fig. 5b. It reflects the recombination rate of electrons and holes during the photoreaction. The smaller arc radius reflects the lower resistance of the interface charge transfer.[49] It is clearly shown that $Bi_4O_5I_2$ has a smaller arc radius, lower chemical impedance and faster charge transport rate. This is consistent with the abovementioned characterization results.

3.9. PL analysis

Photoluminescence (PL) technique was employed herein to further confirm the transfer and recombination of photogenerated electrons and holes for BiOI and $Bi_4O_5I_2$ during the process of photocatalysis. Fig. S3c† shows that $Bi_4O_5I_2$ sample exhibits much lower intensity than BiOI sample, which suggests that $Bi_4O_5I_2$ sample possesses lower recombination rate of the photogenerated charge carriers. It is consistent with the results of PC and EIS analyses.

3.10. Mott–Schottky plot analysis

Mott–Schottky plots (*vs.* SCE) for $Bi_4O_5I_2$ are shown in Fig. S3d.† It is known that the conduction bands of the n-type semiconductors are 0–0.1 eV higher than that of the flat potentials,
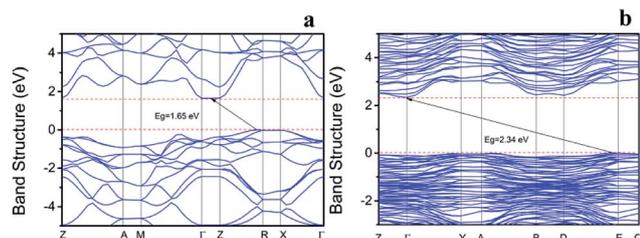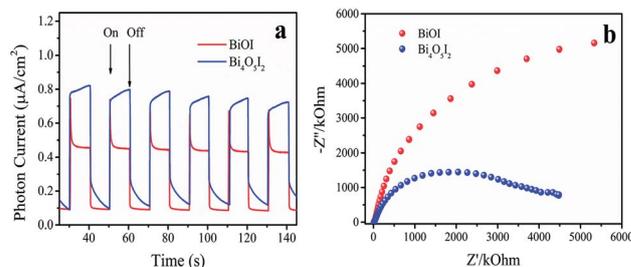

Fig. 4 Band structures of BiOI (a) and $Bi_4O_5I_2$ (b).

Fig. 5 (a) Transient photocurrent spectra and (b) electrochemical impedance spectra of BiOI and $Bi_4O_5I_2$.
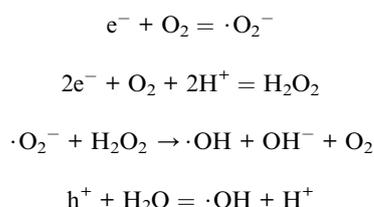
which could be estimated with Mott–Schottky plots. The flat potential is calculated to be -0.75 V *versus* the saturated calomel electrode (SCE), which is equivalent to -0.51 V *versus* the normal hydrogen electrode (NHE). Therefore, the E_{CB} of $Bi_4O_5I_2$ was estimated to be -0.61 eV *vs.* NHE. E_{VB} *vs.* NHE can further be calculated from the equation $E_{VB} = E_g + E_{CB}$, which is estimated to be 1.78 eV *vs.* NHE.

3.11.   Mechanism analysis

Fig. 6 shows a schematic diagram of the band structure and charge migration and separation caused by visible light irradiation. Due to the action of dipole moments, $Bi_4O_5I_2$ non-centrosymmetric polarized structure promotes the separation of photogenerated electron–hole pairs, which leads to efficient photocatalytic activity. On the other hand, based on the trapping and Mott–Schottky experiment, h^+ and $\cdot O^{2-}$ play the role of major active radicals during photodegradation. The possible reason is that a part of $\cdot O^{2-}$ is converted into $\cdot OH$. In addition, E_{CB} of $Bi_4O_5I_2$ is estimated to be -0.61 eV *vs.* NHE, which is lower than that of E_0 ($O_2/O_2^{\cdot -} = -0.046$ eV *vs.* NHE). Therefore, the photogenerated electrons on the CB of $Bi_4O_5I_2$ could be trapped by molecular oxygen to generate $\cdot O^{2-}$ under visible light.

However, its valence band is more negative than E_0 ($OH^-/\cdot OH = 2.38$ eV *vs.* NHE). The result is corresponding to the trapping experiments. The mechanism of the active radical production is proposed as follows:

$$e^- + O_2 = \cdot O_2^-$$

$$2e^- + O_2 + 2H^+ = H_2O_2$$

$$\cdot O_2^- + H_2O_2 \rightarrow \cdot OH + OH^- + O_2$$

$$h^+ + H_2O = \cdot OH + H^+$$

3.12.   PDOS and band-resolved analysis

To clearly understand the essence of photocatalysis and NLO properties, the partial density of states (PDOSs) of $Bi_4O_5I_2$ were
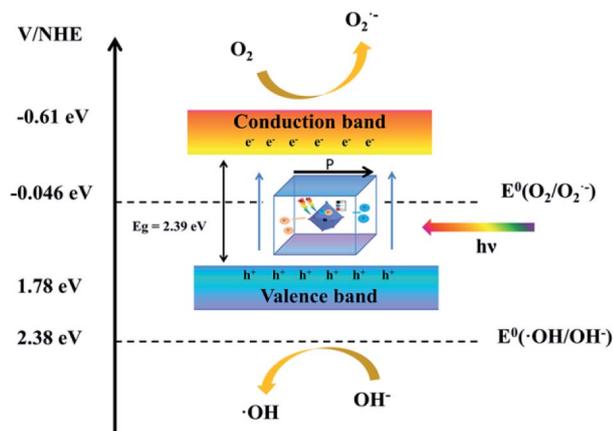

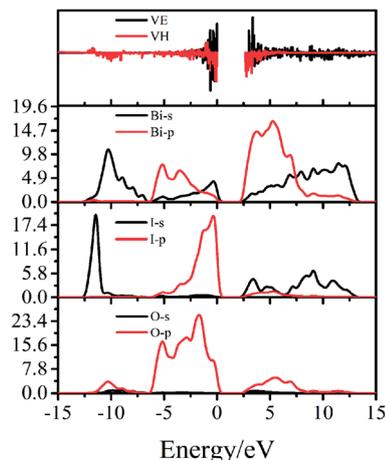**Fig. 7** The PDOS and band-resolved VE and VH processes.

calculated. For $Bi_4O_5I_2$, both the O 2p and I 5p states contributed to the top of the VB and Bi 6p and O 5p states dominated most of the bottom of the CB. The SHG efficiencies are strongly influenced by the direction and the magnitude of the dipole moments of polar structure units.[50] The calculated SHG coefficients of $Bi_4O_5I_2$ are $d_{22} = -7.82$ pm V^{-1} and $\sim$20 KDP (d_{22}) (where KDP, KH_2PO_4, $d_{36} \approx 0.39$ pm V^{-1}, which means it should have large SHG responses). Herein, we considered the SHG efficiencies of $Bi_4O_5I_2$. However, because of the very small size of the $Bi_4O_5I_2$ powder particles, the SHG efficiencies could not be directly accommodated in the experiment. We could not test the results of theoretical predictions experimentally. Therefore, we planned to grow bigger $Bi_4O_5I_2$ crystals and further study and explore the NLO properties of $Bi_4O_5I_2$. In addition, we used the band-resolved method to further explain the contributions of orbitals to the SHG response. The virtual-electron (VE) and virtual-hole (VH) contributions to the total SHG coefficients were obtained. Based on the band-resolved results shown in Fig. 7, these VE and VH contributions are 61.6% and 38.4%, respectively. It indicates that the SHG effect may be due to the VE and VH processes.

4.   Conclusions

In summary, exploration of the versatility of materials to increase the utilization of materials is a hot research topic nowadays. Herein, $Bi_4O_5I_2$ powders have been fabricated *via* a facile solvothermal method. Under the light irradiation for 60 min, 94% of MO and MB were degraded over $Bi_4O_5I_2$ samples. It is noteworthy that for the degradation of methyl orange, the photocatalytic activity of $Bi_4O_5I_2$ is about 10 times that of BiOI. Due to the action of dipole moments, charge separation of the photogenerated electron–hole pairs occurs and thus enhances the photocatalytic activity. In addition, increased dipole moment due to the stereochemical activity of lone pairs induces a high second harmonic generation response. Moreover, theoretical calculation and experiment results reveal that $Bi_4O_5I_2$ would have potential applications in photocatalytic and NLO fields.

Fig. 6 Schematic of the energy band of $Bi_4O_5I_2$ as well as charge migration and separation caused by visible light irradiation.

Conflicts of interest

There are no conflicts of interest to declare.

Acknowledgements

References

1 A. Fujishima and K. Honda, *Nature*, 1972, **238**, 238–245.
2 S. N. Frank and A. J. Bard, *J. Am. Chem. Soc.*, 1977, **99**, 303–304.
3 X. Bai, R. Zong, C. Li, D. Liu, Y. Liu and Y. Zhu, *Appl. Catal., B*, 2014, **147**, 82–91.
4 C. Liu and X. Wang, *Dalton Trans.*, 2016, **45**, 7720–7727.
5 L. Shan, Y. Liu, H. Chen, Z. Wu and Z. Han, *Dalton Trans.*, 2017, **46**, 2310–2321.
6 Y. Huang, B. Long, H. Li, M. Balogun, Z. Rui, Y. Tong and H. Ji, *Adv. Mater. Interfaces*, 2015, **2**, 1500249.
7 Y. Huang, H. Xu, H. Yang, Y. Lin, H. Liu and Y. Tong, *ACS Sustainable Chem. Eng.*, 2018, **6**, 2751–2757.
8 W. Zhong, S. Shen, S. Feng, Z. Lin, Z. Wang and B. Fang, *CrystEngComm*, 2018, **20**, 7851–7856.
9 X. Xiao, C. Zheng, M. Lu, L. Zhang, F. Liu, X. Zuo and J. Nan, *Appl. Catal., B*, 2018, **228**, 142–151.
10 Y. Huang, H. Li, M. Balogun, W. Liu, Y. Tong, X. Lu and H. Ji, *ACS Appl. Mater. Interfaces*, 2014, **6**, 22920–22927.
11 W. Fan, H. Li, F. Zhao, X. Xiao, Y. Huang, H. Ji and Y. Tong, *Chem. Commun.*, 2016, **52**, 5316–5319.
12 Y. Huang, H. Li, W. Fan, F. Zhao, W. Qiu, H. Ji and Y. Tong, *ACS Appl. Mater. Interfaces*, 2016, **8**, 27859–27867.
13 Y. Huang, H. Hu, S. Wang, M. Balogun, H. Ji and Y. Tong, *Appl. Catal., B*, 2017, **218**, 700–708.
14 C. Wang, X. Zhang, X. Song, W. Wang and H. Yu, *ACS Appl. Mater. Interfaces*, 2016, **8**, 5320–5326.
15 Z. Li, M. Wang, J. Shen, Z. Zhu and Y. Liu, *RSC Adv.*, 2016, **6**, 30037–30047.
16 B. B. Adormaa, W. K. Darkwah and Y. Ao, *RSC Adv.*, 2018, **8**, 33551–33563.
17 X. Jing, X. Peng, Y. Cao, W. Wang and S. Wang, *RSC Adv.*, 2018, **8**, 33993–33999.
18 F. Ma, Q. Yang, Z. Wang, Y. Liu, J. Xin, J. Zhang, Y. Hao and L. Li, *RSC Adv.*, 2018, **8**, 15853–15862.
19 S. Garg, M. Yadav, A. Chandra, S. Sapra, S. Gahlawat, P. P. Ingole, Z. Pap and K. Hernadi, *RSC Adv.*, 2018, **8**, 29022–29030.
20 W. Zhong, W. Tu, S. Feng and A. Xu, *J. Alloys Compd.*, 2019, **772**, 669–674.
21 Z. Lin, C. Wang, Z. Wang, Q. Liu, C. Le, B. Lin and S. Chen, *Electrochim. Acta*, 2019, **294**, 142–147.
22 E. Keller, V. Krämer, M. Schmidt and H. Oppermann, *Z. Kristallogr. - Cryst. Mater.*, 2002, **217**, 256–264.
23 X. Xiao and W. Zhang, *RSC Adv.*, 2011, **1**, 1099.
24 W. W. Lee, C.-S. Lu, C.-W. Chuang, Y.-J. Chen, J.-Y. Fu, C.-W. Siao and C.-C. Chen, *RSC Adv.*, 2015, **5**, 23450–23463.
25 Y. Bai, T. Chen, P. Wang, L. Wang and L. Ye, *Chem. Eng. J.*, 2016, **304**, 454–460.
26 C. Ding, L. Ye, Q. Zhao, Z. Zhong, K. Liu, H. Xie, K. Bao, X. Zhang and Z. Huang, *J. CO2 Util.*, 2016, **14**, 135–142.
27 Y. Su, C. Ding, Y. Dang, H. Wang, L. Ye, X. Jin, H. Xie and C. Liu, *Appl. Surf. Sci.*, 2015, **346**, 311–316.
28 X. Wang, Y. Wang, B. Zhang, F. Zhang, Z. Yang and S. Pan, *Angew. Chem.*, 2017, **129**, 14307–14311.
29 X. Xiao, C. Liu, R. Hu, X. Zuo, J. Nan, L. Li and L. Wang, *J. Mater. Chem.*, 2012, **22**, 22840.
30 X. Xiao, C. Xing, G. He, X. Zuo, J. Nan and L. Wang, *Appl. Catal., B*, 2014, **148–149**, 154–163.
31 H. Wu, S. Pan, K. R. Poeppelmeier, H. Li, D. Jia, Z. Chen, X. Fan, Y. Yang, J. M. Rondinelli and H. Luo, *J. Am. Chem. Soc.*, 2011, **133**, 7786–7790.
32 H. Yu, H. Wu, S. Pan, Z. Yang, X. Su and F. Zhang, *J. Mater. Chem.*, 2012, **22**, 9665–9670.
33 H. Wu, H. Yu, Z. Yang, X. Hou, X. Su, S. Pan, K. R. Poeppelmeier and J. M. Rondinelli, *J. Am. Chem. Soc.*, 2013, **135**, 4215–4218.
34 X. Dong, Q. Jing, Y. Shi, Z. Yang, S. Pan, K. R. Poeppelmeier, J. Young and J. M. Rondinelli, *J. Am. Chem. Soc.*, 2015, **137**, 9417–9422.
35 G. Shi, Y. Wang, F. Zhang, B. Zhang, Z. Yang, X. Hou, S. Pan and K. R. Poeppelmeier, *J. Am. Chem. Soc.*, 2017, **139**, 10645–10648.
36 M. Mutailipu, M. Zhang, B. Zhang, L. Wang, Z. Yang, X. Zhou and S. Pan, *Angew. Chem., Int. Ed.*, 2018, **57**, 6095–6099.
37 B. Zhang, G. Shi, Z. Yang, F. Zhang and S. Pan, *Angew. Chem., Int. Ed.*, 2017, **56**, 3916–3919.
38 X. Fan, L. Zang, M. Zhang, H. Qiu, Z. Wang, J. Yin, H. Jia, S. Pan and C. Wang, *Chem. Mater.*, 2014, **26**, 3169–3174.
39 X. Fan, K. Lai, L. Wang, H. Qiu, J. Yin, P. Zhao, S. Pan, J. Xu and C. Wang, *J. Mater. Chem.*, 2015, **3**, 12179–12187.
40 X. Fan, Z. Wu, L. Wang and C. Wang, *Chem. Mater.*, 2016, **29**, 639–647.
41 S. J. Clark, M. D. Segall, C. J. Pickard, P. J. Hasnip, M. I. J. Probert, K. Refson and M. C. Payne, *Z. Kristallogr. - Cryst. Mater.*, 2005, **220**, 567–570.
42 J. P. Perdew and A. Zunger, *Phys. Rev. B*, 1981, **23**, 5048–5079.
43 X. Zhang, Z. Ai, F. Jia and L. Zhang, *J. Phys. Chem. C*, 2008, **112**, 747–753.
44 W. Huang, *J. Comput. Chem.*, 2009, **30**, 1882–1891.
45 S. Qu, Y. Xiong and J. Zhang, *Sep. Purif. Technol.*, 2019, **210**, 382–389.
46 L. Li, L. Xu, W. Shi and J. Guan, *Int. J. Hydrogen Energy*, 2013, **38**, 816–822.
47 J. Xia, J. Di, S. Yin, H. Li, L. Xu, Y. Xu, C. Zhang and H. Shu, *Ceram. Int.*, 2014, **40**, 4607–4616.
48 J. Cao, B. Xu, B. Luo, H. Lin and S. Chen, *Catal. Commun.*, 2011, **13**, 63–68.
49 X. Bai, L. Wang and Y. Zhu, *ACS Catal.*, 2012, **2**, 2769–2778.
50 Z. Yang, C. Hu, M. Mutailipu, Y. Sun, K. Wu, M. Zhang and S. Pan, *J. Mater. Chem. C*, 2018, **6**, 2435–2442.